RESEARCH ARTICLE

ADVANCED MATERIALS INTERFACES Open Access

www.advmatinterfaces.de

Microneedles with Interdigitated Electrodes for In Situ Impedimetric VEGF Sensing

*Ritu Das, Emin Istif, Rumeysa Cebecioglu, Mohsin Ali, Yasin Atik, Çağdaş Dağ, Eda Celikbas, Gozde Demirci, FundaYagcı Acar, Murat Hasanreisoğlu, and Levent Beker**

Continuous monitoring of protein biomarkers in interstitial fluid (ISF) is essential for improving patient care and outcomes. This study presents a novel electrochemical impedance spectroscopy (EIS) sensor utilizing microneedles (MNs) patterned with interdigitated electrodes for the detection of vascular endothelial growth factor (VEGF). The MNs, are fabricated from flexible polylactide (PLA) using a simple molding technique, followed by metal deposition with an interdigitated pattern to serve as a platform for the EIS sensor. After functionalization with anti-VEGF antibodies, impedance measurements are conducted to detect VEGF levels, demonstrating a significant change in impedance in response to varying concentrations of the target biomarker. The MNs can easily penetrate rat skin by hand, puncturing without mechanical breakage. This innovative approach enhances the sensitivity and specificity of biomarker detection and paves the way for continuous monitoring applications in diagnostics and preventative medicine.

1. Introduction

The advent of syringes and hollow needles marked a significant milestone in medical technology, primarily aimed at drug delivery and blood sampling from patients.[1] This innovation was particularly transformative for pharmaceuticals, as many drugs exhibit poor bioavailability when administered orally due to their instability or degradation in the gastrointestinal tract.[1] Despite their continued relevance, the invasive nature of traditional needles, which necessitates skilled healthcare personnel for administration, often leads to discomfort and anxiety among patients. As a result, a new class of minimally invasive technologies has emerged, particularly microneedle-based devices, which offer innovative solutions for drug delivery, diagnostics, and health monitoring applications.

Microneedles (MNs) are designed to penetrate the stratum corneum, allowing for the painless delivery of therapeutic agents or the analysis of biomarkers in interstitial fluid (ISF).[2] The ISF, which shares a high degree of biomarker similarity with blood plasma, provides a rich source for monitoring essential biomarkers with high accuracy and minimal discomfort. This technology has already begun to revolutionize medical treatments, exemplified by the introduction of continuous glucose monitoring systems for diabetic patients, which currently serve ≈415 million individuals worldwide.[3] These devices facilitate ISF sampling and glucose level readings without the need for painful fingerstick blood tests.[4]

The microfabrication of MNs-based biosensing devices represents a burgeoning field, employing various techniques such as

R. Das, E. Istif, Y. Atik, L. Beker
Department of Mechanical Engineering
Koç University
Istanbul 34450, Turkey
E-mail: lbeker@ku.edu.tr

E. Istif
Department of Molecular Biology and Genetics
Faculty of Engineering and Natural Science
Kadir Has University
Istanbul 34083, Turkey

R. Cebecioglu, M. Ali, L. Beker
Department of Biomedical Sciences and Engineering
Koç University
Istanbul 34450, Turkey

Ç. Dağ, L. Beker
Nanofabrication and Nanocharacterization Centre for Scientific and Technological Advanced Research
Koç University
Istanbul 34450, Turkey

E. Celikbas, G. Demirci, F. Acar
Department of Chemistry
Koç University
Istanbul 34450, Turkey

M. Hasanreisoğlu
Department of Opthalmology
School of Medicine
Koç University Hospital
Topkapı caddesi, Zeytinburnu, Istanbul 34010, Turkey

The ORCID identification number(s) for the author(s) of this article can be found under https://doi.org/10.1002/admi.202400789

© 2025 The Author(s). Advanced Materials Interfaces published by Wiley-VCH GmbH. This is an open access article under the terms of the Creative Commons Attribution License, which permits use, distribution and reproduction in any medium, provided the original work is properly cited.

DOI: 10.1002/admi.202400789

micromachining, injection molding, photolithography, and ion-etching.[5–7] While methods like ion etching and photolithography enable the creation of diverse MN types, they often require cleanroom environments, significantly increasing production costs. Conversely, molding techniques present a cost-effective alternative for fabricating polymer-based MNs, utilizing reusable master molds.[6,8,9] MNs can be categorized into two sensing modalities: off-needle and on-needle devices.[10] Off-needle devices extract ISF using hollow MNs for subsequent analysis, but they are limited by their capacity to collect low volumes of fluid.[10] In contrast, on-needle devices utilize solid metal or metal-coated supports as electrodes for electrochemical sensing, relying on interactions such as enzyme-analyte or antibody-antigen binding. However, the requirement for redox mediators to generate signals can hinder their on-body application due to the need for additional reagents. To address these limitations, impedimetric capacitive sensing presents a promising alternative, offering a label-free, non-faradaic platform that does not necessitate redox mediators.[10–14] This approach leverages the dielectric properties and charge distribution changes on the electrodes resulting from bioreceptor-analyte interactions, such as the formation of an electrical double layer.[15] While traditional planar capacitive sensors typically employ interdigitated electrodes and self-assembled monolayers (SAMs) for bioreceptor immobilization, the literature on MN-based interdigitated electrodes remains sparse.

Recent studies have explored the fabrication of capacitive MN arrays for specific biomarker detection. For instance, Song et al. developed a capacitive pillar-type MN array for vascular endothelial growth factor (VEGF) detection, utilizing a silicon wafer processed into micro-pillars through deep reactive-ion etching (DRIE). The sensor monitors the capacitance change between two MNs, which may result in small change due to the small amount of receptors on the sensor needle.[16] However, the rigid structure of silicon-based sensors may limit their practical applications in wearable or in vivo settings due to comfort concerns.

In another study, Wei et al. fabricated MNs with interdigitated electrodes on a flexible substrate, successfully addressing the rigidity issue by employing a parylene substrate and gold-coated silicon MNs.[17] To overcome the rigidity problem of Si-based MNs, the study reports the fabrication of Si needles on a flexible substrate. The final device consists of a parylene flexible substrate and Au-coated Si-based MNs. Nonetheless, the fabrication process involved multiple steps, which could escalate production costs. In light of these challenges, the integration of interdigitated electrodes within microneedles presents a novel approach to enhance the performance of biosensing devices.

This study proposes the development of MNs with interdigitated electrodes (MIdE) specifically designed for in-situ impedimetric sensing of VEGF, a critical biomarker in various clinical conditions. By combining the advantages of minimally invasive sampling with advanced impedimetric sensing capabilities, our approach aims to enhance patient monitoring and treatment outcomes. We utilized polylactide (PLA) as the base material for the MNs, which we created using a molding technique, followed by the deposition of interdigitated gold (Au) electrodes using an evaporation method. To evaluate the device's performance, we functionalized the Au MNs with anti-VEGF antibodies and incrementally introduced VEGF antigens, observing a significant increase in capacitance in response to the target biomarker. This innovative device has the potential to serve as a versatile on-needle sensing system, facilitating the continuous monitoring of various molecules in interstitial fluid (ISF) and paving the way for advancements in diagnostics and personalized medicine.

2. Result and Discussion

2.1. Fabrication of MNs

The MIdE was fabricated using PLA due to its advantageous chemical and mechanical properties, including mechanical flexibility and biodegradability. **Figure 1** illustrates the fabrication process of the microneedle, which incorporates Au interdigitated electrodes for capacitive sensing. This simple micro-molding technique allows for precise control over the structure, shape, and size of each microneedle. The fabrication process consists of five key steps: i) creating a male mold of microneedles using a 3D printer, ii) fabricating a polydimethylsiloxane (PDMS) female mold from the male mold, iii) preparing PLA microneedles by pouring PLA granules into the PDMS mold and heating them to the melting or glass transition temperature, iv) compressing the heated PLA polymer under constant pressure into the PDMS mold, and v) peeling the PLA microneedles from the PDMS mold.

Subsequently, the microneedles were processed to prepare the interdigitated electrodes (IDE) by using a polyimide (PI) hard mask for the deposition of chromium (Cr) and Au via electron beam evaporation. Finally, releasing of PI mask reveals the MIdE structure.

Figure 2 illustrates a manufactured MIdE patch comprising ≈36 solid microneedles per patch arranged in a 7mm x 7mm footprint. Each of the microneedles has a pyramidal shape that is designed using computer-aided drawing program (Figure 2). Once the MNs and MIdEs were fabricated, the structures of the MNs were visualized using optical microscope. (Figure 2; Figure S1, Supporting Information). Figure 2a demonstrates the flexibility of the PLA-based microneedles, which can bend without any deformation or cracking. The microneedle structures were further analyzed post-metal deposition. The MNs structure were also analyzed after the metal deposition. First, MNs was coated with 120 nm of Cr (Figure 2b; Figure S1b–e, Supporting Information) using e-beam evaporation to increase the adhesion of Au on MNs. Finally, the Cr coated MNs was utilized to coat 80 nm of Au (Figure 2c; Figure S1f–h, Supporting Information), which revealed MNs IDE for further use in capacitive sensing applications. The MN samples were rotated inside the evaporation chamber during the deposition of the chromium and gold to ensure uniform metal deposition. The Cr adhesion layer is deposited with 120 nm thickness due to several key factors. First, the microneedle structures possess inherent surface roughness at the microscopic level. A thicker Cr layer ensures complete coverage over these irregularities, providing a uniform and continuous adhesion layer. Thin Cr layers may not adequately cover the rough surfaces, leading to incomplete adhesion and potential defects in the subsequent (Au layer. By increasing the Cr thickness, we ensure that all areas—including microscopic valleys and peaks—are fully coated, which is crucial for the structural integrity and performance of the device. Second, a thicker

© 2025 The Author(s). Advanced Materials Interfaces published by Wiley-VCH GmbH

21967350, 2025, 9, Downloaded from https://advanced.onlinelibrary.wiley.com/doi/10.1002/admi.202400789 by Koc University, Wiley Online Library on [03/09/2025]. See the Terms and Conditions (https://onlinelibrary.wiley.com/terms-and-conditions) on Wiley Online Library for rules of use; OA articles are governed by the applicable Creative Commons License

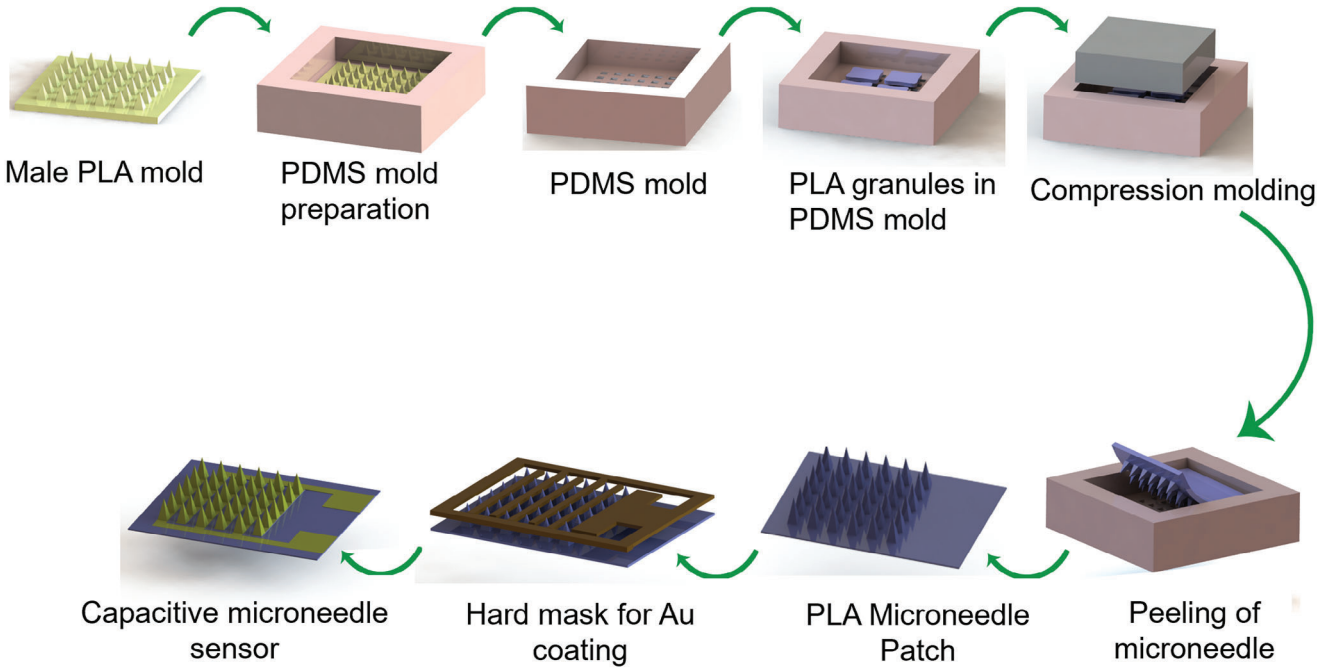


Figure 1. Schematic illustration of the fabrication process for MIdE, which are designed for full insertion into the skin, highlighting their potential applications in biomedical sensing. The diagram outlines the step-by-step assembly of PLA microneedles, beginning with the compression molding of PLA polymer inside a female PDMS mold, followed by the careful peeling of the microneedle patch from the mold. A polyimide hard mask is utilized for the subsequent metal deposition, ensuring precise electrode formation essential for effective capacitive sensing.

Cr layer significantly improves the adhesion between the Au layer and the microneedle structures. In our initial experiments, thinner Cr layers did not provide sufficient adhesion, causing the Au layer to peel off during electrochemical testing. By increasing the thickness of the Cr layer, we effectively prevented this peeling, ensuring the durability and reliability of the microneedles during experiments. Lastly, chromium is prone to oxidation when exposed to aqueous environments during sensing experiments. A very thin Cr layer oxidizes quickly, disrupting its electrical conductivity. This oxidation interferes with the electrical connection between the electrodes and the measurement equipment, resulting in increased noise and unreliable data. A thicker Cr layer reduces the rate of oxidation, maintaining stable conductivity and improving the reliability of the experimental results. These considerations are supported by literature, which highlights the benefits of using a thicker Cr adhesion layer for mechanical stability and improved electrical contact. Studies have shown that Cr can interdiffuse with Au, forming a Cr–Au alloy that enhances the wetting and adhesion between layers, providing superior electrical and physical contact in nano-sized electronic materials.[18–22] Each microneedle has a height of 1.5 mm, with a center-to-center distance of 1.2 mm between adjacent microneedles (Figure 2d).

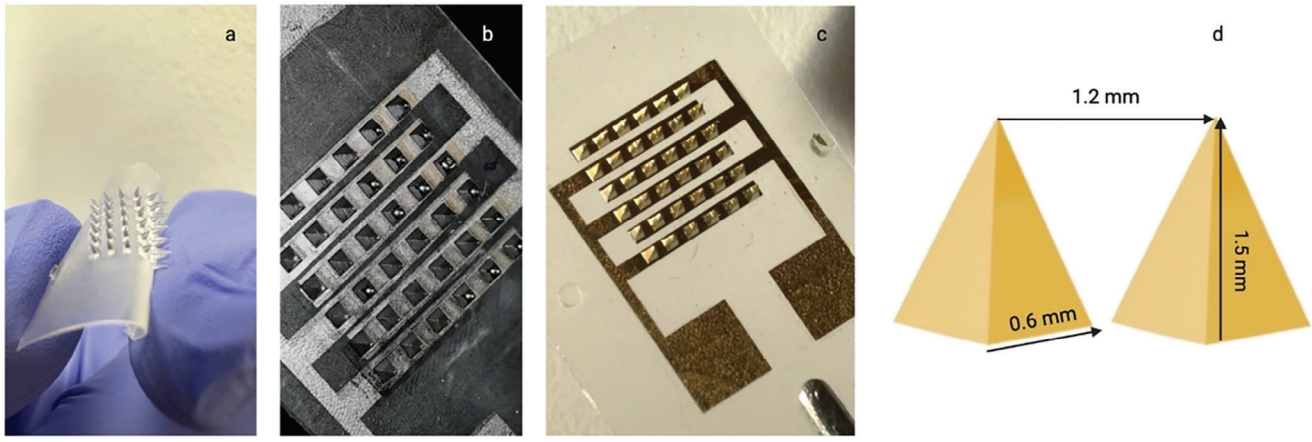


Figure 2. Optical images of the MIdE a) PLA microneedle while bending, b) 120 nm Cr coated MIdE, c) 80 nm Au coated MNs IDE, d) Dimension of a MN.

© 2025 The Author(s). Advanced Materials Interfaces published by Wiley-VCH GmbH

21967350, 2025, 9, Downloaded from https://advanced.onlinelibrary.wiley.com/doi/10.1002/admi.202400789 by Koc University, Wiley Online Library on [03/09/2025]. See the Terms and Conditions (https://onlinelibrary.wiley.com/terms-and-conditions) on Wiley Online Library for rules of use; OA articles are governed by the applicable Creative Commons License

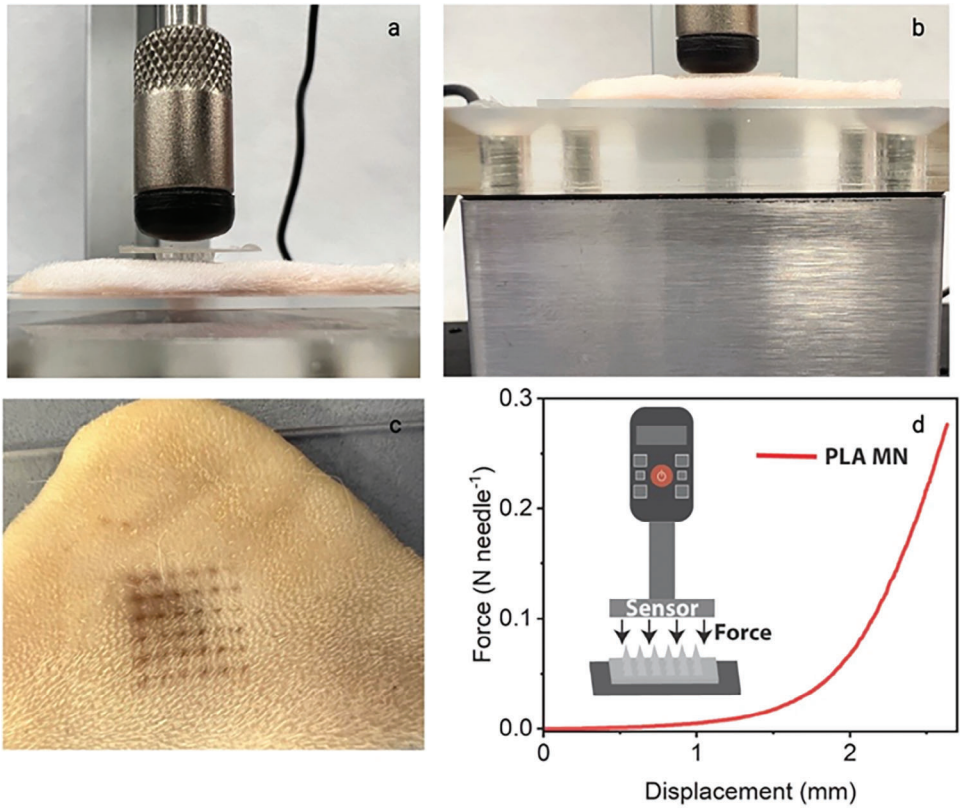


Figure 3. a,b) Optical image of force-displacement test station used to insert microneedle patch into the rat's skin. c) Digital photograph of rat skin after the insertion of a microneedle patch. d) The mechanical behavior of solid PLA microneedles under compression force.

Due to their smooth geometry and fine tips, these microneedles can be quickly injected and fully implanted into the epidermal layer, facilitating rapid skin healing. Multiple sets of microneedles can be inserted into a patient's skin simultaneously, enhancing the efficiency of the procedure.

2.2. Mechanical Properties of MIdE

Investigation of mechanical properties of MNs possess critical importance for future implementation of MNs based sensing devices for biomedical applications. The pressure applied for the insertion of MNs into the skin must be significantly lower than their fracture force to ensure that the needles can withstand the insertion force without breaking. A similar value for insertion and fracture force indicates that the needles may not be strong enough for safe insertion. To evaluate the mechanical performance of the PLA microneedles and their ability to bear the compressive force during insertion, we characterized their mechanical properties using a force gauge setup. The PLA MN can withstand a pressure of 0.275 N per needle (**Figure 3d**), sufficient for penetration into human skin without breaking.[23]

Mechanical testing was performed on uncoated PLA microneedles to evaluate the intrinsic mechanical properties of the base material without the influence of the Cr/Au coating. This approach allows us to assess the fundamental mechanical stability and robustness of the PLA microneedles themselves, ensuring they meet the necessary mechanical requirements for skin penetration and structural integrity. By testing the uncoated microneedles, a clear understanding of the mechanical performance of the PLA material in its native state has been obtained. This is crucial because the primary structural support of the microneedles comes from the PLA substrate. The Cr/Au coating, while adding some minimal thickness, is primarily intended for enhancing electrical conductivity and sensor functionality rather than significantly contributing to mechanical strength. Furthermore, evaluating the mechanical properties of the uncoated microneedles provides a baseline for comparison with coated microneedles, if necessary. It helps in isolating any mechanical effects that may arise solely from the coating process. This information is essential for optimizing the fabrication process and ensuring the reliability and safety of the microneedle device throughout its use, from manufacturing to application. An understanding of the mechanical properties of the uncoated PLA microneedles is critical for confirming their suitability in various stages of device development and for ensuring consistent performance during skin penetration and sensor deployment.

To test the mechanical stiffness of the MN and ensure it has sufficient strength to penetrate the skin, the MN was inserted into the rat skin. The goal was to confirm whether the MN could effectively inserted into the desired location while maintaining its shape without any damage. Figure 3a displays a microneedle patch prior to insertion into rat skin, while Figure 3b illustrates the insertion of a PLA microneedle patch into rat skin under a

 © 2025 The Author(s). Advanced Materials Interfaces published by Wiley-VCH GmbH

21967350, 2025, 9, Downloaded from https://advanced.onlinelibrary.wiley.com/doi/10.1002/admi.202400789 by Koc University, Wiley Online Library on [03/09/2025]. See the Terms and Conditions (https://onlinelibrary.wiley.com/terms-and-conditions) on Wiley Online Library for rules of use; OA articles are governed by the applicable Creative Commons License

10 N force applied through the force gauge. Figure 3c shows an optical image of punctured rat skin, confirming the successful penetration of the MN arrays. The insertion force values obtained in our study align with those reported in previous literature.[24–26] Thus, the results confirmed that the fabricated PLA microneedles in this study could be inserted easily with the hand and puncture the skin without mechanical breakage. Further, to examine whether the PLA microneedle can withstand the shear force, we also performed shear testing of PLA microneedles. The shear testing results suggest that the PLA microneedles exhibit good shear resistance properties upon the application of shear force using a force sensing probe (Figure S3, Supporting Information). Notably, Figure S2 (Supporting Information) shows no damage to the microneedles upon applying a shear force of 0.27 N per needle.

The deposition of a thin Cr/Au layer, ≈200 nm thick, is primarily intended to enhance surface properties such as electrical conductivity and chemical stability, rather than significantly altering the bulk mechanical properties of the PLA matrix. Research indicates that thin metallic films typically do not compromise the structural integrity of polymeric materials, as they mainly contribute to surface characteristics without affecting the overall mechanical strength.[27] The role of the Cr layer is particularly critical as it serves as an adhesion promoter for the Au layer, which cannot bond directly to the PLA surface. This is essential for applications where the MNs are intended to deliver biomolecules effectively. The mechanical strength of the PLA itself is influenced by its inherent properties and the design of the MNs, which are optimized for minimal force application during skin penetration. For instance, the required force for insertion is ≈0.275 N per needle, which is sufficient for effective penetration into human skin without compromising the integrity of the coating. To test the integrity of the Cr/Au coated MN, a skin insertion test was performed using rat skin, and the coated microneedle was checked both before and after its insertion into rat skin (Figure S4a,b, Supporting Information). Additionally, a video demonstrating the successful insertion of the microneedle has been recorded with side and top view confirming the proper insertion of the MN. The video shows that the gold coating remains intact after insertion, with no signs of delamination or damage (SV1 and SV2). Post-insertion, visible markers on the skin confirm effective penetration of the microneedle (Figure S4c, Supporting Information). Furthermore, the structural integrity, sharpness, and coating of the microneedle remain unaffected, providing strong evidence to support the statement that the coating integrity is maintained during and after insertion.

Furthermore, studies on polymer composites have shown that the incorporation of thin metal layers can enhance certain properties, such as electrical conductivity, without significantly diminishing mechanical performance. However, the specific application of MNs, which involves gentle insertion rather than high-stress applications, suggests that the Cr/Au coating will remain intact under typical usage conditions.

2.3. Fabrication and Characterization of Capacitive MIdE

To demonstrate a capacitive biosensing application, a VEGF sensor utilizing Au coated MIdE was developed to detect VEGF levels. VEGF, a key protein in angiogenesis associated with diseases like cancer and diabetic retinopathy, was targeted.[28–31] Thiol-functionalized VEGF antibodies (anti-VEGF) were immobilized on Au MNs through overnight incubation at 4 °C in a flow cell. The incubated solution underwent sodium dodecyl sulfate-polyacrylamide (SDS) characterization to confirm anti-VEGF binding to the Au MNs. Next, the incubated solution was collected from the cell and used for SDS characterization to observe a bounded amount of anti-VEGF to Au MNs. The collected incubated sample (FS), control sample, and anti-VEGF stock solution were subjected to electrophoresis using a 12% SDS page. The control sample and the stock solution of the anti-VEGF showed a prominent band at ≈20 kD. The FS sample showed a clear band at approximately ≈20 kD (**Figure 4a**). This result confirmed that the anti-VEGF are immobilized to the Au MNs surface.

The Bradford protein assay was also employed to quantify the concentration of anti-VEGF in the incubation samples collected during the experiment. Bovine serum albumin (BSA) standards, with concentrations ranging from 0 to 1 mg mL^{-1}, were utilized to construct a calibration curve. The absorbance values of BSA standards and anti-VEGF samples which was collected from incubation solutions were measured at 595 nm. A linear relationship between the absorbance and concentration was observed for the BSA standards (R^2 = 0,98), providing a reliable calibration curve for the quantification the residual anti-VEGF after functionalization. The VEGF protein concentration of the collected incubation sample was calculated using the calibration curve. The calculated VEGF protein concentration in the collected sample was 0.104 mg mL^{-1}, compared to a stock solution concentration of 0.29 mg mL^{-1}. Consequently, the binding ratio of the VEGF protein was determined to be 69% based on the calibration curve.

The electrochemical characterization of functionalized MIdE was performed using cyclic voltammetry (CV) and electrochemical impedance spectroscopy (EIS) after confirming the functionalization of the VEGF antibody. For electrochemical measurements, while one of the MNs used as working and the other for the counter electrode, Ag/AgCl electrode was connected to the setup externally. Electrochemical characterization was conducted in 5mM K_3FeCN_6 solution in 0.1 M KCl. Figure 4b shows the CV results of a functionalized electrodes using anti-VEGF, BSA, and VEGF. The bare electrode CV was given in the probe (Figure S5, Supporting Information), which showed the current range ≈0,12 mA. After anti-VEGF functionalization on Au MNs, the CV result shows that the maximum current for oxidation peak decreases to 0125 µA due to the formation of a protein insulating layer over the Au MNs. The antibody layer on Au MNs prevents the effective charge transfer, which results in a decrease in current value. After using BSA as a surface-blocking layer to prevent non-specific binding, the maximum oxidation current decreases to ≈0075 µA, which shows that the antibody-free surface of Au MNs is covered with the BSA insulating layer. Further, 1 ng of VEGF was incubated over the functionalized electrode to analyze the current change. Increasing the thickness of the insulating layer due to the binding of antibody-antigen relation, the peak current continues to decrease, as observed in case of antibody and BSA. The CV results confirm the decreasing efficiency of charge-transfer processes between the interface of Au MNs and electrolyte due to formation of insulating layers.

© 2025 The Author(s). Advanced Materials Interfaces published by Wiley-VCH GmbH

21967350, 2025, 9, Downloaded from https://advanced.onlinelibrary.wiley.com/doi/10.1002/admi.202400789 by Koc University, Wiley Online Library on [03/09/2025]. See the Terms and Conditions (https://onlinelibrary.wiley.com/terms-and-conditions) on Wiley Online Library for rules of use; OA articles are governed by the applicable Creative Commons License

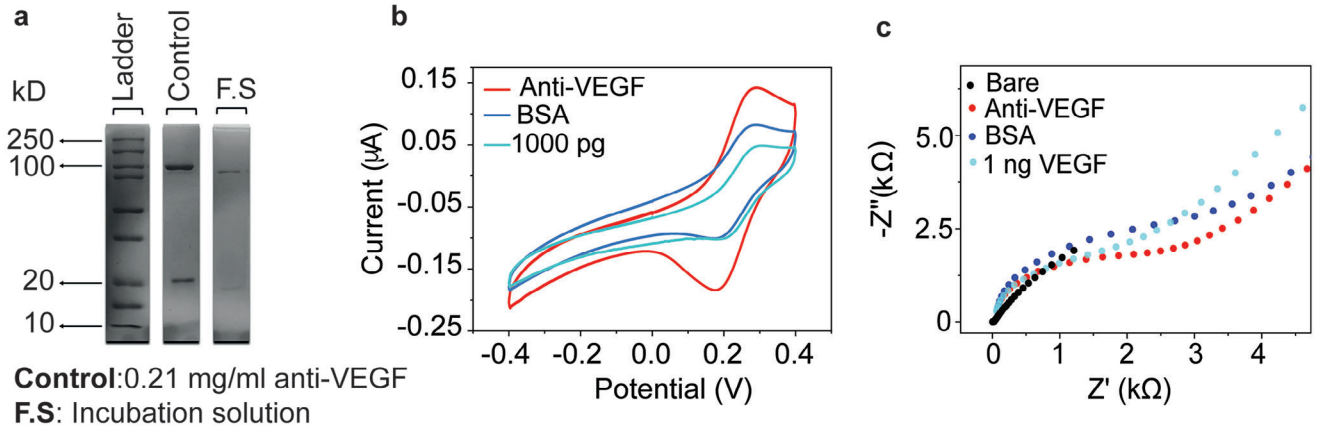


Figure 4. a) SDS-Page analysis of VEGF protein, b) CV of the sensor in 5mM K_3FeCN_6 solution in 0.1 M KCl after anti-VEGF and 1 ng of VEGF incubation, c) EIS characterization of the bare and functionalized electrodes in 5mM K_3FeCN_6 solution in 0.1 M KCl.

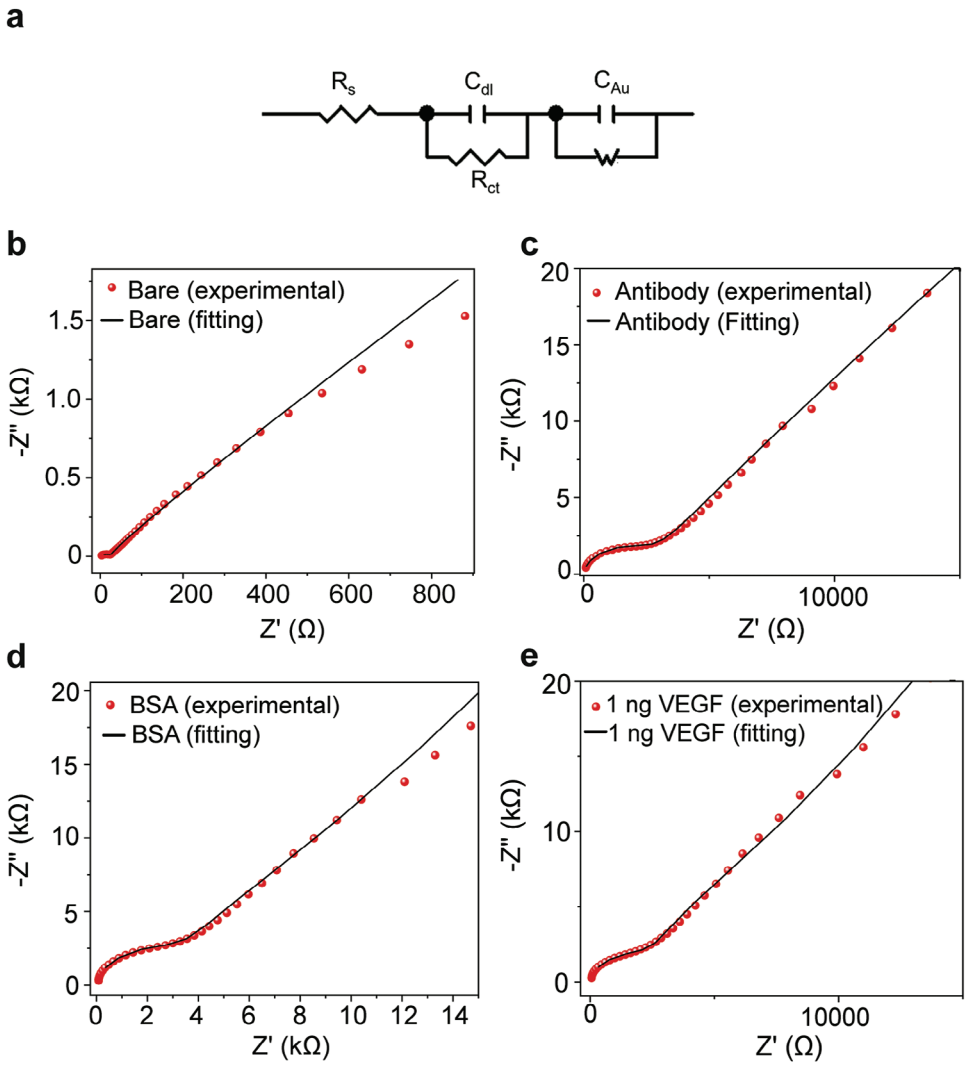


Figure 5. a) Schematic diagram of an equivalent circuit model. b–e) Nyquist plot of the electrode, which is represented by overlapping the experimental and fitted results.

© 2025 The Author(s). Advanced Materials Interfaces published by Wiley-VCH GmbH

21967350, 2025, 9, Downloaded from https://advanced.onlinelibrary.wiley.com/doi/10.1002/admi.202400789 by Koc University, Wiley Online Library on [03/09/2025]. See the Terms and Conditions (https://onlinelibrary.wiley.com/terms-and-conditions) on Wiley Online Library for rules of use; OA articles are governed by the applicable Creative Commons License

Table 1. Obtained R_s and R_{ct} values after fitting the Nyquist plot.

Electrode	R_s Values	R_{ct} Values
Bare MNs	3434	20,37
Antibody functionalized	27,3	2564
BSA functionalized	51,09	3311
1 ng VEGF	47,97	2335

EIS experiment was also conducted to measures the impedance value after each sample incubation. EIS spectrum was taken in a wide frequency range between 10 Hz to 500 kHz. The results show that upon incubation of each protein, the linear Au response changed to the semicircular and linear part, which indicates the different charge-transfer and diffusion-controlled processes. Therefore, EIS results also confirm the binding of antibody and BSA to Au surface and antigen to antibody. To understand the sensing mechanism, the equivalent circuit models were extracted for the bare and functionalized sensor. Since EIS characterization of the bare and functionalized electrodes were conducted in 5mM K_3FeCN_6 solution in 0.1 M KCl. Faradaic impedance spectra were obtained from the Nyquist results which involve both the semicircle (shows that electrochemical process is controlled by charge transfer phenomena) and the inclined straight line (shows that the electrochemical process is controlled by mass transfer phenomena).[32] The interdigitated electrodes based on MNs presented here offer a unique configuration for faradaic impedance spectroscopy, and no related studies have yet been published to explore the equivalent circuit model for this specific design.

The equivalent circuit model of the sensing system was extracted by simulating the results using Z-View software (Z view v.3.1c, Scribner Associates) (**Figure 5a**). The best-fitted model for each electrode modification step is also given in Figure 5(b–e). The extracted faradaic impedimetric parameters are the Warburg impedance (W), which is associated with the impedance related to the electrolyte's ions or molecules diffusing toward the electrode surface, the charge transfer resistance (Rct) which is related with the charge transfer rate of the redox reaction at the interface of the electrode, (Cdl) represent the double layer capacitor, (Rs) is the solution resistance (Rs), and (CAu) refers to the interfacial capacitance of interdigitated gold MNs.

We hypothesize that, as similarly reported in the literature[33] for interdigitated electrodes, the equivalent circuit model consists of two parts:i) Interfacial part: Represented by RctR_{ct}Rct (charge transfer resistance) and CdlC_{dl}Cdl (double-layer capacitance), arising from the organic layer formation at the interface due to the functionalization of antibodies and antigens. ii) Inner part: Represented by the ideal capacitive behavior of the Au MNs electrode and a Warburg element, which accounts for the straight line observed at low frequencies due to ion or molecular diffusion. Since the diameter of the semi-circle is proportional to Rct, and provides insight about the functionalization of the electrode and antibody-antigen binding, the Rct parameters are shown in **Table 1**. As expected, once the organic layer formed on the surface of the electrodes Rct level increased compared to the bare MNs electrode.[33]

Once SDS and electrochemical analysis confirmed the antibody immobilization and antigen binding, capacitance measurements were conducted for bare and functionalized Au MNs to reveal the implementation of MIdE for the capacitive sensing.

Impedance measurements were conducted using an impedance analyzer (IA) (MFIA, Zurich Instruments) in 1 x PBS solution. After incubation of each sample, the sensor was rinsed with PBS and placed in a flow cell (Figure S6, Supporting Information). The impedance measurement was conducted by adding ≈200 uL of PBS over the electrode and measuring the capacitance in the range of 100 Hz to 1MHz. **Figure 6a** shows the capacitance results of different samples. The capacitance response was measured under the same condition. The results exhibit that functionalization of Au with anti-VEGF, and BSA increases capacitance in the range of 100 Hz to 10 kHz. Next, the dose-response behavior of our capacitive MNs sensor toward VEGF was evaluated across a broad concentration range of 100 pg mL^{-1} to 1 ng mL^{-1}. This range was determined due to the anticipated levels of VEGF in the biological samples of interest.[34–36] The sensor's response, as quantified by changes in capacitance, and the response was recorded for each concentration of VEGF. We observed that the incremental addition of VEGF leads to an increase in capacitance response (Figure 6a), The calibration curve for VEGF detection, shown in Figure 6b, indicates a linear range from 100 to 1000 pg mL^{-1} VEGF (based on S/N = 3) with the limit of detection (LOD) of 100 pg mL^{-1} and sensitivity 0.47 nF $^{-1}$pg $^{-1}$$mL^{-1}$. The standard deviation (σ) was calculated as the standard deviation of the blank signal (i.e., the capacitance values measured in the absence of the target analyte, i.e., VEGF). Multiple replicates (n = 3) of the blank measurements were performed to ensure statistical reliability. The resulting standard deviation represents the inherent noise or variability in the system when no analyte (VEGF) is present.

The LOD was then calculated using the formula:

$$\text{LOD} = \frac{3 \times \sigma}{\text{sensitivity}} \quad (1)$$

where the sensitivity was determined from the slope of the calibration curve, calculated as 0.458 nF/pg·mL. Using this approach, the LOD was calculated to be 100 pg mL^{-1}. This methodology aligns with standard practices for LOD determination in sensor development and ensures the reproducibility and accuracy of the reported value.[37] The studies compared with the current method have been discussed in detail in Section S1 (Supporting Information). A comparison table of VEGF sensors has been summarized in Table S1 (Supporting Information), representing the performance of different biosensors for VEGF in the literature.

Further, the selectivity of the capacitive MIdE was tested using several interfering substances, including epidermal carcinoembryonic antigen (CEA), myoglobin (Myg), and ascorbic acid (AA) (Figure 6c). Before performing the selectivity, the frequency with the maximum capacitance change was determined with 500 pg mL^{-1} of VEGF for maximum sensor response. Since 1 kHz frequency shows the highest change for the capacitive response, we calculated the percent capacitance change for 1 kHz using the following equation ($C\text{-}C_0/C_0 x100$). At 1 kHz, the sensor exhibited a 6% capacitance change when incubated with 500

© 2025 The Author(s). Advanced Materials Interfaces published by Wiley-VCH GmbH

21967350, 2025, 9, Downloaded from https://advanced.onlinelibrary.wiley.com/doi/10.1002/admi.202400789 by Koc University, Wiley Online Library on [03/09/2025]. See the Terms and Conditions (https://onlinelibrary.wiley.com/terms-and-conditions) on Wiley Online Library for rules of use; OA articles are governed by the applicable Creative Commons License

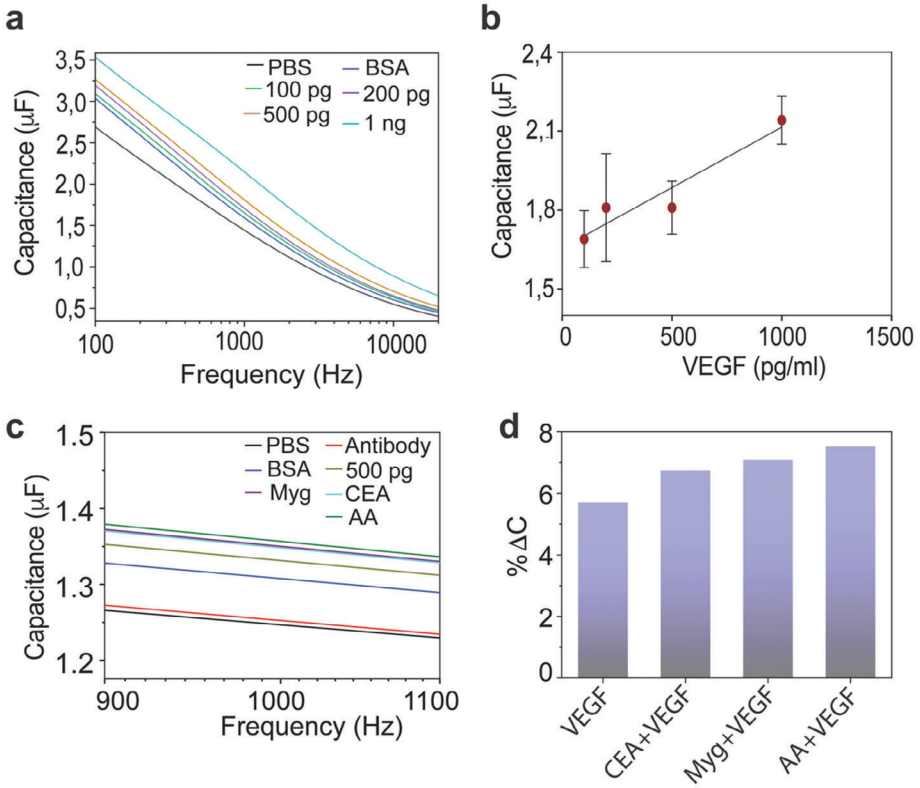


Figure 6. a) Capacitance responses of the sensor at different concentrations of VEGF protein, b) Calibration curve of VEGF for 100, 200, 500, and 100 pg mL^{-1} in 1X PBS. c) Capacitance response of the sensor with interfering substances, d) Percentage change in capacitance of the sensor with interfering substances.

pg mL^{-1} VEGF, confirming its high sensitivity to the VEGF. Further, to determine the selectivity of the sensor in the presence of the potential interfering substance, 1ng/ml of VEGF protein was mixed with 10ng/ml of the interfering substance, and the capacitance response was measured. The results show a maximum 2% change in the capacitance in the presence of the interfering substance, indicating minimal cross-reactivity (Figure 6d). The change in capacitance can be due to the unsaturated anti-VEGF Ab on the Au MNs, which remain highly specific to VEGF even in the complex mixture. The results show the high selectivity behavior of the sensor, showcasing its ability to sensitively detect the VEGF even in the presence of the interfering substance, making it suitable for application in complex biological environments.

3. Conclusion

The presented microfabrication technique for flexible MIdE with Au interdigitated arrays offers significant advancements in in situ capacitive sensing technology. The MNs demonstrate excellent flexibility and resilience, ensuring no breakage during application on rat skin, which is crucial for future wearable sensor implementations that prioritize user comfort. The sensor's performance was effectively validated through capacitance monitoring across various VEGF concentrations, revealing a direct correlation between increased VEGF levels and capacitance increase. This in situ on-needle sensing method circumvents the complexities associated with traditional sampling systems, facilitating pain-free and minimally invasive continuous monitoring of protein biomarkers. The potential applications of this technology in wearable biomedical devices could significantly enhance diagnostic and therapeutic practices, ultimately improving patient care. Future research should focus on optimizing the sensor's sensitivity and specificity for broader clinical applications.

4. Experimental Section

Reagents: Anti-VEGF was isolated from Bevacizumab drug (Altuzan, Roche 400 mg/16 mL) and used for thiol modification. Recombinant Human VEGF-165 (Animal-Free) was purchased from BioLegend (10 mg). VEGF-165 dissolved in PBS, aliquoted, and stored at −78 °C.PBS was purchased from Biowest, AASO10H1007. Carcinoembryonic Antigen (CEA), Myoglobin, Cardiac troponin- I (cTn-I) were purchased from HyTest, Finland and, L-Ascorbic acid was purchased from Sigma–Aldrich, A92902, USA. Isopropyl alcohol (IPA) was purchased from TEKKIM, 67 630, Turkey and, Potassium ferricyanide (K_3FeCN_6) was purchased from Sigma–Aldrich, 244 023, USA.

To determine the protein concentration of anti-VEGF, incubated solutions were recovered and analyzed using Bradford Protein Assay (Thermo Scientific, WK342279, USA). Coomassie Plus Protein reagent (Thermo Scientific, 1 856 210, USA) was used as a reagent. Bovine serum albumin (BSA) (Thermo Scientific, WI334017, USA) was diluted at 1 mg mL^{-1} in PBS and was used for the calibration curve. BSA was diluted at 10;20;50;100;200;300, and 400 ug mL^{-1} in PBS to make a calibration curve.

Fabrication of PLA MNs: The microneedle male mold was prepared by the (3D printer Boston Micro Fabrication (BMF) S230), which was further utilized to fabricate female molds using Polydimethylsiloxane (Dow Corning). To fabricate a patch of polylactic acid (PLA) microneedle

© 2025 The Author(s). Advanced Materials Interfaces published by Wiley-VCH GmbH

21967350, 2025, 9, Downloaded from https://advanced.onlinelibrary.wiley.com/doi/10.1002/admi.202400789 by Koc University, Wiley Online Library on [03/09/2025]. See the Terms and Conditions (https://onlinelibrary.wiley.com/terms-and-conditions) on Wiley Online Library for rules of use; OA articles are governed by the applicable Creative Commons License

(MN), PLA pellets were manually compression molded into an MN structure inside a PDMS mold at melting temperature; PLA pellets were poured into the PDMS mold at its melting temperature or glass transition temperature and wait until the pellets start turning into the rubbery form. Then, the flexible form PLA pellets were compressed by putting a constant weight on the PDMS mold for 5–7 min so that the polymer could quickly fill the MN mold area. After that, the PDMS mold was allowed to cool at room temperature, followed by removing the PLA MN patch from the PDMS mold. The microneedles were arranged in a 6 × 6 array with a center-to-center interval of 1200 µm in an area of 7 mm × 7 mm, and each microneedle was pyramidal with a height of 1.5 mm. The distance between two microneedles is 0.6 mm. After removing the PLA MN patch from the PDMS mold, metal deposition is done. Thin films of Cr and Au with 120 and 80 nm thicknesses were deposited using the Kurt J. Lesker EB-PVD 75 e-beam physical vapor deposition system from the Kurt J. Lesker Company located in Pittsburg, PA, USA. The deposition process was performed on PLA MN patches overlaid with thin sheets of Polyimide (PI) masks that were precisely designed to resemble an interdigitated capacitor layout. These masks were fabricated by cutting out patterns from a large PI sheet using a UV [355-nm] laser ablation system [LPKF; Protolaser U4]. The deposition was conducted with Cr thin film being deposited first, followed by Au thin film without removing the samples from the e-beam evaporator. The pressure was maintained at 1×10^{-5} Pa during the deposition, and no specific heating was applied. The deposition rate ranged from 0.6 to 0.8 A s^{-1}.

Mechanical Properties Experimentation: A force–displacement test station (Force Gauge; Mark-10) was used to measure the mechanical properties of PLA microneedles (Figure 2d). Briefly, for compression testing of microneedle patches, a microneedle patch was attached to a flat rigid stage, keeping the tip of the microneedles up. The test stage with the microneedle patch approached the sensor probe tip (flat surface) with a speed of 0.1 mms^{-1}. Before starting the test, the distance between the microneedle tips and the sensor was 1 mm. Force and displacement values started increasing after touching the microneedle tips, and it continued until the sensor covered 1.6 mm from the microneedle tips to the backing of the patch.

Shear testing of microneedles was also conducted utilizing FemtoTools (FT-MTA03, AG, Zurich, Switzerland). The microneedle patch was attached with the help of double-sided tape, keeping the tip of the microneedles up on the 3-axis piezo scanner of FemtoTools. FemtoTools micro force sensing technology based on FT-S force sensing probe, which combines outstanding accuracy and flexibility, was utilized to apply the shear force on the microneedle. The upper part of the microneedle (from the base of the microneedle patch) was sheared through the micro force sensing probe at a height of 0.5 mm from the base. The force sensor applied shear force at the rate of 1.2 µm s^{-1}, and data were sampled at 43 samples per second. The shear testing data was utilized to plot a relationship between shear force per needle as a function of displacement of the shared surface of the microneedle.

Fabrication of Capacitive Sensing Microneedle: Metal deposition on the PLA MNs was performed using a polyimide-based hard mask with interdigitated electrode design 26ort he deposition of Cr and Au. Electron beam evaporation (PVD 200 Pro-line, Kurt J. Lesker) was utilized to deposit metal electrodes. A 120 nm thick layer of chromium metal was deposited first on the PLA microneedle patch. This Chromium electrode layer serves as an adhesion layer for the gold coating. Subsequently, an 80 nm thick layer of Au was deposited on the Cr adhesion layer by e-beam deposition.[17,27]

Electrochemical Measurements: Capacitive sensing measurements were performed in an Impedance Analyzer (MFIA, Zurich Instrument). Capacitance changes were measured in the frequency range of 100 Hz to 1MHz using an impedance analyzer 26ort he bare MNs, functionalized MNs and after the incremental addition of VEGF doses. Capacitance and impedance values were exported to Excel (Microsoft Office 365, version 2304) and plotted using Origin (Origin 9.0, 64 bit).

Sensor Functionalization: The functionalization of the sensors was conducted in three steps. First, the MNs surface was cleaned with ethanol (EtOH), isopropanol (IPA) and deionized (DI) water, respectively and incubated in PBS overnight to stabilize the capacitance change. Then, the capacitance measurements of bare MNs were obtained using an impedance analyzer. In the second step, the MNs were incubated with an anti-VEGF solution at 0,21 mg mL^{-1} overnight. The anti-VEGF solution was removed in the third stage, and capacitance was measured in PBS. To prevent the non-specific binding a blocking layer was formed on the surface using BSA (1 mg mL^{-1}) and incubated at room temperature for 30 min. Following BSA incubation, the BSA solution was removed, and PBS solution was added to run capacitance measurement. Subsequently, dose-response experiments were performed by adding VEGF proteins at 100, 200, 400, 600, 800, 1000, and 1200 pg mL^{-1}, respectively. Each antigen was incubated for 1 h. After each addition of antigen, the surface was gently washed with PBS, and capacitance measurements were recorded in PBS solution. Sensor functionalization and analysis are illustrated in Figure S7 (Supporting Information).

Selectivity Experiment: For the selectivity test, the MNs were cleaned as described in the previous section. To this end, interference molecules such as CEA, Myoglobin, L-Ascorbic acid, and CTnI were added to the sensors. Each interference molecule was incubated for 1 h, and capacitance was measured in PBS. The frequency values during the capacitance measurement were set between 100 Hz and 1 MHz.

In the first step of the selectivity tests, the microneedle sensors were incubated overnight with 0,21 mg mL^{-1} of anti-VEGF. After overnight incubation, the anti-VEGF solution was replaced with PBS, and impedance measurement was carried out to record the capacitance of the functionalized microneedle electrodes. The sensors were incubated with 1 mg mL^{-1} of BSA for 30 min at room temperature to form a blocking layer on the sensor surfaces. After the incubation, the BSA solution was replaced with PBS, and impedance measurement was carried out. Once the anti-VEGF and BSA immobilization were completed, interference proteins were added for selectivity testing. First, VEGF protein was incubated at a 500 pg mL^{-1} concentration for 1 h. The protein solution was replaced with fresh PBS, and capacitance values were measured using an impedance analyzer. Next, solutions were prepared for each interference protein, with 1 ng mL^{-1} concentration for the VEGF protein and 10 ng mL^{-1} for the interference protein. Each solution was incubated for 1 h before being replaced with fresh PBS, and capacitance values were measured in PBS.

Bradford Protein Assay: The concentration of the VEGF antibody protein in the incubation solutions was determined using plastic polymethylmethacrylate (PMMA) cuvette. First, BSA standards were prepared at different concentrations (10, 20, 50, 100, 200, 300, and 400 ug mL^{-1}). Afterward, incubation solutions were diluted, and samples were prepared for analysis. When the BSA and samples were prepared, 500 µL of each sample was taken and mixed with 500 µL of Coomassie plus protein reagent. Subsequently, samples and standards were ready for measurement with a UV Spectrophotometer at 575 nm.

SDS-Page: To conduct the SDS-Page experiment, two different gels were prepared: separating and stacking gels. A 12% separating gel was prepared by combining 3.9 mL of 30% acrylamide/8% bis solution, 2.437 mL of 1.5 M Tris-HCl (pH 8.8), 3.9 mL of ultrapure water, 97.5 µL of 10% SDS, 48.75 µL of 10% ammonium persulfate (APS), and 4.875 µL of N,N,N', N'-tetramethylethylenediamine (TEMED). The gel solution was poured into the gel assembly, and a spacer was placed on top to allow the gel to polymerize. After polymerization, a 12% stacking gel was prepared by mixing 0.67 mL of 30% acrylamide/bis solution, 1.3 mL of 0.5 M Tris-HCl (pH 6.8), 2.93 mL of ultrapure water, 50 µL of 10% SDS, 50 µL of 10% APS, and 5 µL of TEMED. The stacking gel was poured on top of the separating gel, and a comb was inserted to create wells.

Supporting Information

Supporting Information is available from the Wiley Online Library or from the author.

Acknowledgements

L.B. acknowledges TUBITAK 2232 (grant no. 118C295) and the European Research Council (2ND-CHANCE, grant no. 101043119). The authors

© 2025 The Author(s). Advanced Materials Interfaces published by Wiley-VCH GmbH

21967350, 2025, 9, Downloaded from https://advanced.onlinelibrary.wiley.com/doi/10.1002/admi.202400789 by Koc University, Wiley Online Library on [03/09/2025]. See the Terms and Conditions (https://onlinelibrary.wiley.com/terms-and-conditions) on Wiley Online Library for rules of use; OA articles are governed by the applicable Creative Commons License

acknowledge Koç University Surface Science and Technology Center (KUYTAM) and Koç University Nanofabrication and Nanocharacterization Center (n2STAR) for access to the infrastructure.

Conflict of Interest

The authors declare no conflict of interest.

Author Contributions

M.A. and Y.A. designed the microneedles, masks and fabricated microneedles with interdigitated electrodes. M.A. characterized the mechanical properties of the MNs and carried out optical images experiments. E.I. and R.C. fabricated and characterized the VEGF sensor. Ç.D. performed the SDS page experiments. E.C. and G.D. prepared the thiol modified VEGF antibody. R.D. and E.I. analyzed and interpreted the data and drafted the article. F.Y.A. and M.H. contributed to the drafting and revision of the article. L.B. contributed to the preparation of MNs with interdigitated electrodes, the development of the sensor, data interpretation, and the drafting and revision of the article.

Data Availability Statement

The data that support the findings of this study are available from the corresponding author upon reasonable request.

Keywords

biosensor, capacitive, microneedle, VEGF

Received: October 3, 2024
Revised: December 3, 2024
Published online: January 9, 2025

[1] D. V McAllister, M. G. Allen, M. R. Prausnitz, *Ann. Rev. Biomed. Eng.* **2000**, *2*, 289.
[2] Y.-C. Kim, J.-H. Park, M. R. Prausnitz, *Adv. Drug Delivery Rev.* **2012**, *64*, 1547.
[3] G. H. R. Rao, *Diab. Obes. Int. J.* **2018**, *3*, 1.
[4] M. Krakauer, J. F. Botero, F. J. Lavalle-González, A. Proietti, D. E. Barbieri, *Diabetol. Metab. Syndr.* **2021**, *13*, 42.
[5] R. K. Mishra, K. Y. Goud, Z. Li, C. Moonla, M. A. Mohamed, F. Tehrani, H. Teymourian, J. Wang, *J. Am. Chem. Soc.* **2020**, *142*, 5991.
[6] S. Sharma, A. Saeed, C. Johnson, N. Gadegaard, A. E. Cass, *Sens. Biosens. Res.* **2017**, *13*, 104.
[7] A. M. V. Mohan, J. R. Windmiller, R. K. Mishra, J. Wang, *Biosens. Bioelectron.* **2017**, *91*, 574.
[8] K. Badnikar, S. N. Jayadevi, S. Pahal, S. Sripada, M. M. Nayak, P. K. Vemula, D. N. Subrahmanyam, *Macromol. Mater. Eng.* **2020**, *305*, 2070011.
[9] J.-H. Park, M. G. Allen, M. R. Prausnitz, *J. Controlled Release* **2005**, *104*, 51.
[10] S. Odinotski, K. Dhingra, A. GhavamiNejad, H. Zheng, P. GhavamiNejad, H. Gaouda, D. Mohammadrezaei, M. Poudineh, *Small* **2022**, *18*, 2200201.
[11] A. Qureshi, Y. Gurbuz, J. H. Niazi, *Sens. Actuators B Chem.* **2015**, *209*, 645.
[12] C. Berggren, B. Bjarnason, G. Johansson, *Electroanalysis* **2001**, *13*, 173.
[13] H. Sun, Y. Zheng, G. Shi, H. Haick, M. Zhang, *Small* **2023**, *19*, 2207539.
[14] K. Liu, H. Wang, F. Zhu, Z. Chang, R. Du, Y. Deng, X. Qi, *ACS Nano* **2024**, *18*, 14207.
[15] C. Robinson, V. B. Juska, A. O'Riordan, *Electrochem. Impedance Spectrosc.* **2022**, https://chemrxiv.org/engage/chemrxiv/article-details/62822e8b44bdd51f26650d67.
[16] S. Song, J. Na, M. Jang, H. Lee, H.-S. Lee, Y.-B. Lim, H. Choi, Y. Chae, *IEEE Trans. Biomed. Circuits Sys.* **2019**, *13*, 1288.
[17] Z. Wei, S. Zheng, R. Wang, X. Bu, H. Ma, Y. Wu, L. Zhu, Z. Hu, Z. Liang, Z. Li, *Lab Chip* **2014**, *14*, 4093.
[18] D. V. McAllister, P. M. Wang, S. P. Davis, J. H. Park, P. J. Canatella, M. G. Allen, M. R. Prausnitz, *Proc. Natl. Acad. Sci. U. S. A.* **2003**, *100*, 13755.
[19] Y. Wu, F. Tehrani, H. Teymourian, J. Mack, A. Shaver, M. Reynoso, J. Kavner, N. Huang, A. Furmidge, A. Duvvuri, Y. Nie, L. M. Laffel, F. J. Doyle, M. E. Patti, E. Dassau, J. Wang, N. Arroyo-Currás, *Anal. Chem.* **2022**, *94*, 8335.
[20] N. Song, P. Xie, W. Shen, H. Oh, Y. Zhang, F. Vitale, M. Javanmard, M. G. Allen, *Microsyst. Nanoeng.* **2021**, *7*, 96.
[21] M. Todeschini, A. B Da Silva Fanta, F. Jensen, J. B. Wagner, A. Han, *ACS Appl. Mater. Interfaces* **2017**, *9*, 37374.
[22] B. L. Zhang, Y. Yang, Z. Q. Zhao, X. D. Guo, *Electrochim. Acta* **2020**, *358*, 136917.
[23] S. P. Davis, B. J. Landis, Z. H. Adams, M. G. Allen, M. R. Prausnitz, *J. Biomech.* **2004**, *37*, 1155.
[24] N. V Apollo, J. Jiang, W. Cheung, S. Baquier, A. Lai, A. Mirebedini, J. Foroughi, G. G. Wallace, M. N. Shivdasani, S. Prawer, S. Chen, R. Williams, M. J. Cook, D. A. X. Nayagam, D. J. Garrett, *Adv. Biosyst.* **2017**, *2*, 1700187.
[25] P. Makvandi, A. Maleki, M. Shabani, A. R. J. Hutton, M. Kirkby, R. Jamaledin, T. Fang, J. He, J. Lee, B. Mazzolai, R. F. Donnelly, F. R. Tay, G. Chen, V. Mattoli, *Matter* **2022**, *5*, 390.
[26] P. Makvandi, M. Kirkby, A. R. J. Hutton, M. Shabani, C. K. Y. Yiu, Z. Baghbantaraghdari, R. Jamaledin, M. Carlotti, B. Mazzolai, V. Mattoli, R. F. Donnelly, *Nanomicro Lett.* **2021**, *13*, 93.
[27] L. Liu, M. Zhu, X. Xu, X. Li, Z. Ma, Z. Jiang, A. Pich, H. Wang, P. Song, *Adv. Mater.* **2021**, *33*, 2105829.
[28] P. Osaadon, X. J. Fagan, T. Lifshitz, J. Levy, *Eye* **2014**, *28*, 510.
[29] Y. Zhao, R. P. Singh, *Drugs Context* **2018**, *7*, 1.
[30] C. Kut, F. Mac Gabhann, A. S. Popel, *Br. J. Cancer* **2007**, *97*, 978.
[31] E. R. Gerstner, D. G. Duda, E. di Tomaso, P. A. Ryg, J. S. Loeffler, A. G. Sorensen, P. Ivy, R. K. Jain, T. T. Batchelor, *Nat. Rev. Clin. Oncol.* **2009**, *6*, 229.
[32] A. C. Lazanas, M. I. Prodromidis, *ACS Measur. Sci. Au* **2023**, *3*, 162.
[33] M. Kim, R. Iezzi, B. S. Shim, D. C. Martin, *Front. Chem.* **2019**, *7*, 444510.
[34] M. O. Stefanini, F. T. H. Wu, F. Mac Gabhann, A. S. Popel, *BMC Syst. Biol.* **2008**, *2*, 77.
[35] T. Cabral, L. H. Lima, J. Polido, J. Duong, É. Okuda, A. Oshima, P. Serracarbassa, C. V Regatieri, R. Belfort Jr, *Int. J. Retina Vitreous* **2017**, *3*, 6.
[36] M. Kim, R. Iezzi Jr, B. S. Shim, D. C. Martin, *Front. Chem.* **2019**, *7*, 234.
[37] D. Echeverri, M. Garg, D. Varón Silva, J. Orozco, *Talanta* **2020**, *217*, 121117.

© 2025 The Author(s). Advanced Materials Interfaces published by Wiley-VCH GmbH

21967350, 2025, 9, Downloaded from https://advanced.onlinelibrary.wiley.com/doi/10.1002/admi.202400789 by Koc University, Wiley Online Library on [03/09/2025]. See the Terms and Conditions (https://onlinelibrary.wiley.com/terms-and-conditions) on Wiley Online Library for rules of use; OA articles are governed by the applicable Creative Commons License